

RESEARCH ARTICLE

10.1002/2016GC006270

Key Points:

- Spatial patterns of mineral transformation were revealed from measurements of aqueous geochemistry
- Rapid weathering resulted in supersaturation with respect to short-range ordered precipitates
- Suspended neoformed nanoparticles were an important pathway for transport of Fe, Al, and P

Supporting Information:

- Supporting Information S1

Correspondence to:

J. Chorover,
chorover@email.arizona.edu

Citation:

Pohlmann, M., K. Dontsova, R. Root, J. Ruiz, P. Troch, and J. Chorover (2016), Pore water chemistry reveals gradients in mineral transformation across a model basaltic hillslope, *Geochem. Geophys. Geosyst.*, 17, 2054–2069, doi:10.1002/2016GC006270.

Received 22 JAN 2016

Accepted 1 MAY 2016

Accepted article online 9 MAY 2016

Published online 18 JUN 2016

Corrected 18 JULY 2016

This article was corrected on 18 JUL 2016. See the end of the full text for details.

Pore water chemistry reveals gradients in mineral transformation across a model basaltic hillslope

Michael Pohlmann¹, Katerina Dontsova², Robert Root¹, Joaquin Ruiz^{2,3}, Peter Troch^{2,4}, and Jon Chorover^{1,2}

¹Department of Soil, Water and Environmental Science, University of Arizona, Tucson, Arizona, USA, ²Biosphere 2, University of Arizona, Tucson, Arizona, USA, ³Department of Geosciences, University of Arizona, Tucson, Arizona, USA, ⁴Department of Hydrology and Water Resources, University of Arizona, Tucson, Arizona, USA

Abstract The extent of weathering incongruity during soil formation from rock controls local carbon and nutrient cycling in ecosystems, as well as the evolution of hydrologic flow paths. Prior studies of basalt weathering, including those that have quantified the dynamics of well-mixed, bench-scale laboratory reactors or characterized the structure and integrated response of field systems, indicate a strong influence of system scale on weathering rate and trajectory. For example, integrated catchment response tends to produce lower weathering rates than do well mixed reactors, but the mechanisms underlying these disparities remain unclear. Here we present pore water geochemistry and physical sensor data gathered during two controlled rainfall-runoff events on a large-scale convergent model hillslope mantled with 1 m uniform depth of granular basaltic porous media. The dense sampler and sensor array (1488 samplers and sensors embedded in 330 m³ of basalt) showed that rainfall-induced dissolution of basaltic glass produced supersaturation of pore waters with respect to multiple secondary solids including allophane, gibbsite, ferrihydrite, birnessite and calcite. The spatial distribution of saturation state was heterogeneous, suggesting an accumulation of solutes leading to precipitation of secondary solids along hydrologic flow paths. Rapid dissolution of primary silicates was widespread throughout the entire hillslope, irrespective of up-gradient flowpath length. However, coherent spatial variations in solution chemistry and saturation indices were observed in depth profiles and between distinct topographic regions of the hillslope. Colloids (110–2000 nm) enriched in iron (Fe), aluminum (Al), and phosphorus (P) were mobile in soil pore waters.

1. Introduction

The formation of secondary minerals from incongruent weathering of silicate rock is central to biogeochemical processes in the critical zone, including those that impact global scale climate [Berner *et al.*, 1983; Dupré *et al.*, 2003]. These dissolution, nucleation and crystal growth processes occurring at the grain and pore scale [Brantley *et al.*, 2006, Chorover *et al.*, 2007, Navarre-Sitchler and Brantley, 2007], significantly affect the global carbon cycle [Berner *et al.*, 1983; Gislason *et al.*, 1996; Stefansson and Gislason, 2001; Dessert *et al.*, 2003; Suchet *et al.*, 2003; Gislason *et al.*, 2009]. Continental weathering of Ca-Mg silicates conveys Ca²⁺ (from dissolution of primary rock) and HCO₃⁻ (from dissolution of gaseous CO₂) to the oceans where calcite and aragonite are deposited [Gislason *et al.*, 2009; Gurumurthy *et al.*, 2012]. Basaltic silicates exhibit rapid dissolution kinetics because of their volcanic glass and nesosilicate-dominated mineralogy [Gislason and Arnorsson, 1993; Oelkers and Gislason, 2001; Bluth and Kump, 1994]. Hence, despite having relatively limited global distribution compared to other lithologies (5% of earth's land area), basalt silicates are a substantial contributor to the sequestration of atmospheric carbon dioxide (CO₂) over geologic time scales, accounting for 7% of total CO₂ uptake, and nearly 30% of the uptake associated with silicate weathering in particular [Gaillardet *et al.*, 1999; Dessert *et al.*, 2003; Suchet *et al.*, 2003].

Inputs of freshwater that drive weathering reactions on the continents, act as both solvent and transport vector for dissolved and particulate weathering products [Gaillardet *et al.*, 1999; Gislason *et al.*, 1996]. In pedogenic environments, throughput of fresh water in contact with primary mineral surfaces leads to rock dissolution and increase in pore water saturation with respect to secondary aluminosilicates, metal (oxy)-hydroxides and carbonates. Neo-formed poorly crystalline solids (e.g., microcrystalline gibbsite, allophane and ferrihydrite) exhibit reactive surfaces that enhance their interaction with the matrix via surface

precipitation and colloidal adhesion, thereby reducing their mobility. Precipitating solids can passivate the surfaces of primary minerals against further dissolution [Stumm, 1997] and contribute to the stabilization of organic carbon and plant-available nutrients [Torn et al., 1997; Chorover et al., 2004]. Water-soluble elements (e.g., Na) tend to leach down gradient toward riverine and marine sinks [Chadwick and Chorover, 2001]. In more advanced weathering, the development and accumulation of secondary phases in the smallest size fraction (e.g., 2:1 layer-type clays and colloids), leads to alteration of the soil structure via pore-filling, aggregation and associated macropore formation [Christensen, 2001; Bronick and Lal, 2005]. Increasingly crystalline secondary phases are formed over longer time scales, as predicted by Ostwald ripening whereby less-crystalline, higher solubility, and higher surface area particles are transformed to increasingly crystalline phases of greater size and stability, and lower aqueous solubility [Steefel and van Cappellen, 1990].

Numerous field studies have attempted to calculate weathering rates and effects on global scale biogeochemical processes using riverine solutes [Bluth and Kump, 1994; Louvat and Allègre, 1997; Stefansson and Gislason, 2001; Benedetti et al., 2003; Dupré et al., 2003; Suchet et al., 2003; Dessert et al., 2003; Gislason et al., 2009]. Discernment of solutes as a weathering signal must account for up-gradient lithology, morphology, hydrologic flow paths, vegetative cover, climate (including meteoric water inputs), and incorporate a detailed understanding of reactive surface area within a catchment. Conversely, laboratory determined mineral weathering rates can be orders of magnitude higher than those calculated from watershed chemical discharges – a difference resulting, in part, from shorter fluid residence times, higher reactive surface area, and higher temperatures of laboratory studies relative to field conditions [Oelkers, 2001; Oelkers and Gislason, 2001; Gislason and Oelkers, 2003; Wolff-Boenisch et al., 2004; Dontsova et al., 2014]. Indeed, accurate accounting of reactive surface area is often indicated when examining disparities between lab and field scale weathering rates [White and Peterson, 1990; Swoboda-Colberg and Drever, 1993].

The Landscape Evolution Observatory (LEO) constructed at Biosphere 2 in Tucson, AZ (USA) is a model hillslope in controlled environment that seeks to bridge the gap between field and lab scale studies to better understand the array of interacting hydrologic, geochemical and biological processes that drive hillslope evolution – including silicate mineral weathering – and their impact on the carbon cycle [Pangle et al., 2015]. Like a laboratory reactor, LEO offers a high degree of environmental control and a high density of monitoring capability, but it enables studies on a spatial scale more characteristic of a small watershed. This makes it an ideal tool to investigate hillslope-scale coupling of hydrologic and biogeochemical processes in an initially isotropic and homogeneous system anticipated to develop in complexity and heterogeneity over the decadal time scale of climate-controlled evolution [Hopp et al., 2009; Dontsova et al., 2009; Pangle et al., 2015].

In the present study, pore water geochemistry and sensor data sets from two initial rainfall events were used to obtain a detailed understanding of spatial and temporal changes occurring in the earliest stage of granular basalt weathering. We hypothesized that progressive accumulation of basalt-derived solutes along hydrologic flowpaths would elevate aqueous geochemical saturation index values to those indicative of secondary solid precipitation. We also hypothesized that some portion of element mass released by mineral dissolution may nucleate secondary precipitates that occur as mobile colloids, nonetheless contributing to geochemical translocation and denudation of the hillslope.

2. Materials and Methods

2.1. Basaltic Porous Medium

LEO includes three replicated convergent hillslope structures, constructed as zero order basins (each 330 m² in size) with 1 m depth of porous media composed of granular basalt. The facility enables climate-control for each hillslope housed in separate bays. Results presented here pertain to the LEO east hillslope, the first instrument constructed and subject to initial experimentation [Gevaert et al., 2014; Niu et al., 2014; Pangle et al., 2015]. The south facing steel framed structures are each 30 m long, 11 m wide and 1 m deep, accommodating 330 m³ of crushed basalt tephra installed to a uniform (1 m) depth (Figure 1).

The basalt was obtained near Flagstaff, Arizona from a >30 m thick late Pleistocene volcanic deposit associated with the Merriam Crater [Duffield et al., 2006]. It was ground on site to achieve the desired loamy sand particle size distribution (Table 1) prior to packing to a target bulk density (ρ_b) of 1.59 g cm⁻³ during the concurrent installation of basalt and instrumentation (sensors and samplers) [Gevaert et al., 2014]. Chemical,

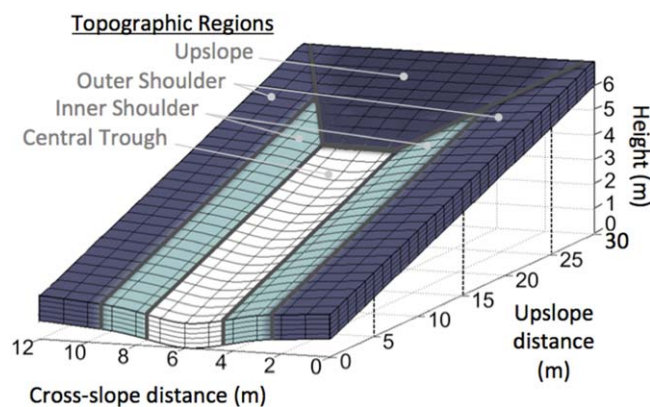


Figure 1. Schematic of the Landscape Evolution Observatory hillslope (not to scale) highlighting the demarcation of topographic regions discussed in text (upslope, outer shoulder, inner shoulder and central trough). Convergence and slope (10° average) convey water and solutes toward the seepage face (vertical cross section shown at bottom of structure).

mineralogical and physical data on the porous basaltic material presented previously [Dontsova et al., 2009; Pangle et al., 2015] are summarized in Table 1. Electron microprobe analysis of the basalt medium (Figure 2) showed evidence of labradorite, forsterite, diopside, and titanomagnetite crystals of different sizes embedded in basaltic glass matrix. Backscattered electron micrographs of the basalt show sharp and diverse particle geometries with a high prevalence of vesicularity that creates substantive internal porosity (Figure 2). Vesicles range from 100 nm (determined by N₂ absorption using Barrett-Joyner-Halenda (BJH) theory [Barrett et al.,

1951]) up to 100 μm in diameter (as seen on the backscatter images). Postprocessing particle size analysis confirmed a low clay-size contribution, ca. 32 g kg⁻¹ as required for the target hydraulic conductivity (θ_{sat}) of 1.92 m d⁻¹ [Gevaert et al., 2014]. Low content of fine particles should reduce the signal to noise of incipient secondary mineral nucleation and growth, supporting the detection of neo-formed particles that occupy the smallest size fractions. The initially homogeneous and isotropic medium will be monitored for 10 years as continued water inputs and eventual introduction of vascular plants contribute to the development of subsurface differentiation and heterogeneity. Although the hillslopes are nonsterile, initial organic carbon (OC) inputs are low (0.07 g kg⁻¹ ± 0.01 CI) [Pangle et al., 2015].

2.2. Sensor and Sampler Array

Real-time sensors of gas and liquid phase dynamics (measuring PCO₂, temperature, pressure head, and volumetric water content) are embedded at 0.05, 0.2, 0.35, 0.5, 0.85 m depth throughout the 1 m profile, with horizontal spacing between nested sensor clusters of 2.0 m in downslope direction and 1.0 m across the slope. Also embedded in the hillslope are 496 custom Prenart SuperQuartz soil-water samplers (2 microm pore size, Prenart Equipment ApS, Frederiksberg, Denmark), colocated with 5TM sensors (Decagon, Pullman, WA, USA) for measuring temperature and volumetric water content (VWC) (supporting information Figure S1). Topography is that of a simple convergent hillslope with an average slope of 10° (maximum slope: 17°) that conveys water and solutes toward a central trough and through a seepage face that drains into tipping buckets for outflow mass balance measurement (Figure 1). Each steel structure is lined with urethane membranes over concrete board, providing an inert impermeable boundary at the base of the “soil” profile. Paired sprinklers positioned along the long edges of the slope distributed reverse osmosis (RO) purified water to the contoured surface of the hillslope. Following equilibration with atmospheric CO₂ and prior to

Table 1. Basalt Tephra Characterization^a

Primary Phases (Mineral)	Composition	Weight % ± SE
Basaltic glass	Ca _{0.44} Mg _{0.30} Na _{0.26} K _{0.06} Mn _{0.01} Fe _{0.38} Al _{0.62} Ti _{0.07} (HPO ₄) _{0.03} Si _{1.80} O _{5.93} ^b	57.8 ± 1.8
Feldspar (Labradorite)	Ca _{0.69} Mg _{0.01} Fe _{0.04} Na _{0.3} K _{0.01} Al _{1.64} Si _{2.32} O ₈	23.4 ± 1.5
Olivine (Forsterite)	Mg _{1.64} Ca _{0.01} Fe _{0.33} SiO ₄	12.6 ± 0.4
Pyroxene (Diopside)	Ca _{0.86} Mn _{0.01} Mg _{0.78} Na _{0.03} Ti _{0.05} Al _{0.22} Fe _{0.27} Cr _{0.01} Si _{1.81} O ₆	5.3 ± 1.3
Oxide (Titanomagnetite)	Fe _{2.31} Mg _{0.26} Ca _{0.02} Mn _{0.02} Cr _{0.01} Al _{0.18} Ti _{0.49} Si _{0.06} O ₄	1.0 ± 1.0
Particle Sizes	Diameter Range (mm)	Weight % ± SE
Sand	50-2000	84.6 ± 0.20
Silt	2-50	12.2 ± 0.16
Clay	< 2	3.2 ± 0.03

^aAfter Pangle et al. [2015].

^bOxide mass concentrations (g kg⁻¹): SiO₂ = 484.1, Al₂O₃ = 141.5, FeO = 122.2, CaO = 110.5, MgO = 54.1, Na₂O = 36.1, TiO₂ = 25.0, K₂O = 12.7, MnO = 3.2, P₂O₅ = 9.5.

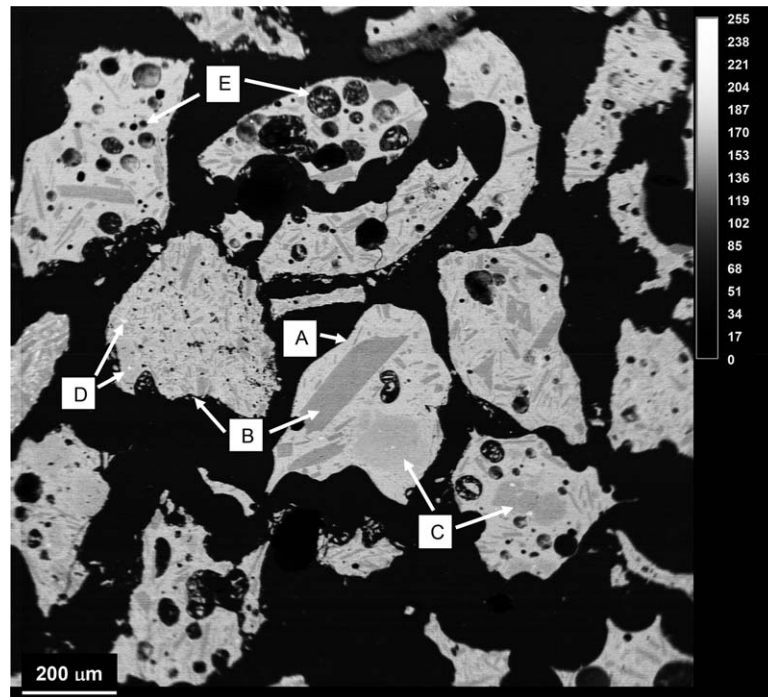


Figure 2. Back-scattered electron image of the Flagstaff basalt used in the LEO experiment (Cameca SX-50 electron microprobe, 15 kV accelerating voltage, 20 nA sample current, a beam size of 2 μm). Samples were embedded in epoxy resin and polished to a 0.75 μm finish. Letters indicate: A—basaltic glass, B—labradorite, C—forsterite, D—titanomagnetite; E—vesicles. Diopside while present in the rock is not visible on this image. Highly visible in black are vesicular pores in the 1–100 μm diameter range that are widely distributed throughout the media with some larger porosity resulting from pore interconnection.

contacting the basaltic hillslope, RO water had a pH 5.4 and low contaminant ion concentrations (Table 2). Rainfall intensity was controlled with an electromagnetic flow meter in the irrigation line.

2.3. Irrigation and Sample Collection

Following hillslope installation and initial prewetting, two rain events were applied to LEO east in February and April 2013, respectively, and these events are the focus of this study (Table 2). The February event (R1) lasted 22 h with an intensity of 12 mm hr⁻¹, totaling ca. 16.4 cm of rainfall depth, and a total water volume of 87.12 m³. Saturation of the central trough and lower reaches of the hillslope coupled with limited drainage contributed to the development of subsurface lateral and eventually overland flow at approximately 13–14 h after the start of irrigation [Gevaert *et al.*, 2014; Niu *et al.*, 2014]. On DOY 50, irrigation was terminated after overland flow developed. A more conservative irrigation scheme was executed in April (R2), which resulted in no detectable overland flow. A series of three pulses of rain at 12 mm hr⁻¹ was executed: DOY 102, 103 and 111, distributing a total of 64.8 m³ (ca. 74% of the volume applied in R1 to a hillslope that

Table 2. Sampling Schedule and Irrigation Details

Rain Event	Duration (Intensity)	Collection DOY	Sample Count		
R1: DOY 49	22 hrs (12 mm h ⁻¹)	50	30		
Single irrigation total: 87,740 L		51	30		
		52	244 ^a		
		53	30		
		59	176 ^a		
R2: DOY 102	6 hrs × 3 (12mm h ⁻¹)	113	200		
Series irrigation total: 64,840 L ^b		115	205		
Irrigation Water ^c					
pH	DIC	Na	K	Mg	Ca
5.44	44.19	65.94	2.41	1.03	4.25

^aIncludes same 30-sample selection as DOY 50, DOY 51, and DOY 53.

^bSeries Irrigation (12 mm h⁻¹ intensity): DOY 102 (22,400 L), DOY 103 (23,050 L), DOY 111 (19,390 L).

^cConcentrations for DIC and cations in μmol L⁻¹.

had a time zero total volume of water equal to 25 m³). This latter time zero water content was comparable to the water content present at time zero of rainfall for R1 (31 m³).

2.3.1. Initial 30-Location Sampling

An initial survey of pore waters from 30 locations throughout the hillslope was conducted upon cessation of R1 on DOY 50, and continued for DOY 51, 52, 53 and 59 (i.e., 150 samples total samples). The 30 locations were chosen to provide samples from all regions and depths, and to coincide with samples collected by *Gevaert et al.* [2014]. To test the hypothesis of colloid mobilization, pore water samples (with porous samplers comprising a 2000 nm pore size) were each split into noncentrifuged (NC) and high-speed centrifuged (HSC) aliquots. Comparison of NC and HSC aliquots would identify the occurrence of material within the 110 nm to 2000 nm size range (see section 2.4). This experimental run was also conducted to provide an overview of the hillslope chemistry, and to assess time-dependent change in pore water solute concentrations in a range of hillslope positions spanning 9 days following termination of rainfall.

2.3.2. Whole-Hillslope Sampling

Whole-hillslope sampling was conducted to examine pore water total concentrations in which all samplers producing water were collected throughout the hillslope following R1 and R2 to enable a detailed view of the spatial variability for solutes and predicted secondary phases. Whole-hillslope collections were conducted on DOY 52 (n = 244) and DOY 59 (n = 176) following R1, and DOY 113 (n = 200) and DOY 115 (n = 205) following R2.

With the initial survey and whole-hillslope sampling, a total of 915 pore water samples were collected following R1 and R2 (Table 2). Pore waters were collected from the samplers with tensioned syringes via Teflon tubing, set with a pin to hold the piston and maintain suction (ca. 2.9 kPa) during solution collection. Samples were transferred into 50 mL polypropylene metal free tubes and stored at 4° C until further processing and analysis. Since solution volumes for a given sampler were sometimes insufficient for the full suite of geochemical analyses, sampling involved compositing two rounds of collection the same day to ensure adequate sample mass. Since sensors collect readings continuously at 15 min intervals, whereas pore water were collected at two discrete times, average values for sensor data from the two sampling times for temperature (T) and volumetric water content (VWC) were employed in data analysis and modeling. The applied RO rainwater at LEO contributed minimally to pore water chemistry (Table 2), indicating measured pore water constituents were derived from dissolution of the basalt.

2.4. Sample Preparation and Analysis

Pore water samples were subjected to centrifugation using a Sorvall Legend XTR (ThermoFisher, Waltham, MA) at 4816 relative centrifugal force (RCF) for 20 min, removing particles of equivalent spherical diameter (according to Stoke's Law) from 110 to 2000 nm (assuming 3.96 g cm⁻³ particle density as for Fe oxides) or 150–2000 nm (assuming 2.65 g cm⁻³ particle density as for aluminosilicates) [*Whittig et al.*, 1986], and before-after centrifugation chemical analyses enabled testing for the presence of neo-formed mobile colloids. Since the pore water samplers themselves disallow particles >2000 nm, the designated colloidal fraction for this experiment ranged from 110 to 2000 nm. Following centrifugation, samples were aspirated into 15 mL metal free tubes and kept at 4° C until chemical analysis at the B2 Biogeochemistry Laboratory and at the Arizona Laboratory for Emerging Contaminants (ALEC) on the University of Arizona campus. Anions (F⁻, Cl⁻, NO₂⁻, Br⁻, NO₃⁻, SO₄²⁻, and PO₄³⁻) were analyzed on a DIONEX ICS-5000 fitted with an IonSwift MAX-100 capillary and guard column (Thermo-Fisher Waltham, MA). Total and organic carbon analysis was conducted using a Shimadzu TOC-L (Columbia, MD). The pH was measured using a SymPHony SB90M5 pH probe (VWR, Radnor, PA). Cations were analyzed using a Perkin Elmer ELAN DRC II or Agilent 7700 ICP-MS outfitted with a dynamic reaction cell to eliminate molecular interferences, after being diluted using 1% Omni-trace nitric acid.

2.5. Geochemical Modeling

Aqueous geochemical data were used as input to a thermodynamic model (Geochemists Workbench [GWB], Version 10, Champagne-Urbana, IL) to calculate aqueous phase speciation and saturation index (SI) values of solutions with respect to a wide range of potentially precipitating secondary solids [*Bethke*, 2011]. Measured temperature and analytical geochemistry data sets were input into SpecE8, the aqueous chemistry module for GWB. Thorough geochemical analyses were used in conjunction with basis species including H⁺, HCO₃⁻, F⁻, Cl⁻, NO₂⁻, NO₃⁻, SO₄⁻, Na⁺, Mg²⁺, Al³⁺, SiO_{2(aq)}, K⁺, Ca²⁺, V³⁺, Cr²⁺, Mn²⁺, Fe³⁺, Co³⁺, Ni²⁺, Cu²⁺, Zn²⁺, As(OH)₄⁻, Sr²⁺, Ba²⁺, O_{2(aq)} and critical stability constants to calculate major and trace species in solution for all analytical components measured for the LEO pore waters. A total of 655 samples from

Table 3. Thermodynamic Data^a

Mineral Name	Dissolution Reaction	Log K		
		0 C	25 C	60 C
<i>Manganese Oxides</i>				
Birnessite	$\text{Mn}_8\text{O}_{19}\text{H}_{10} + 16\text{H}^+ = 8\text{Mn}^{2+} + 13\text{H}_2\text{O} + 3\text{O}_{2(\text{aq})}$	12.39	11.68	10.67 ^b
Pyrolusite	$\text{MnO}_2 + 2\text{H}^+ = \text{Mn}^{2+} + \text{H}_2\text{O} + 0.5\text{O}_{2(\text{aq})}$	-1.54	-1.44	-1.25
<i>Aluminosilicates and Aluminum Hydroxide</i>				
Proto-imogolite allophane	$(\text{OH})_3\text{Al}_2\text{O}_3\text{SiOH} + 6\text{H}^+ = 2\text{Al}^{3+} + \text{SiO}_2 + 5\text{H}_2\text{O}$	8.57 ^{c,d}	7.02 ^c	5.24 ^{c,d}
Mg-Montmorillonite	$\text{Mg}_{0.495}\text{Al}_{1.67}\text{Si}_4\text{O}_{10}(\text{OH})_2 + 6\text{H}^+ = 0.495\text{Mg}^{2+} + 1.67\text{Al}^{3+} + 4\text{SiO}_2 + 4\text{H}_2\text{O}$	3.60	2.39	0.16
Heulandite	$\text{CaAl}_2\text{Si}_7\text{O}_{18}(\text{H}_2\text{O})_6 + 8\text{H}^+ = \text{Ca}^{2+} + 2\text{Al}^{3+} + 7\text{SiO}_2 + 10\text{H}_2\text{O}$	4.36	2.88	0.75
Kaolinite	$\text{Al}_2\text{Si}_2\text{O}_5(\text{OH})_4 + 6\text{H}^+ = 2\text{Al}^{3+} + 2\text{SiO}_2 + 5\text{H}_2\text{O}$	9.73	7.43	4.76
Analcime	$\text{NaAlSi}_2\text{O}_5(\text{H}_2\text{O}) + 4\text{H}^+ = \text{Na}^+ + \text{Al}^{3+} + 2\text{SiO}_{2(\text{aq})} + 3\text{H}_2\text{O}$	8.62	7.28	5.67
Gibbsite	$\text{Al}(\text{OH})_3 + 3\text{H}^+ = \text{Al}^{3+} + 3\text{H}_2\text{O}$	9.52	7.96	6.25
<i>Iron Oxyhydroxides</i>				
Ferrihydrite	$\text{Fe}(\text{OH})_3 + 3\text{H}^+ = \text{Fe}^{3+} + 3\text{H}_2\text{O}$	6.19	4.89	3.46
Goethite	$\text{FeOOH} + 3\text{H}^+ = \text{Fe}^{3+} + 2\text{H}_2\text{O}$	1.51	0.50	-0.61
<i>Calcium Carbonate</i>				
Calcite	$\text{CaCO}_3 + \text{H}^+ = \text{Ca}^{2+} + \text{HCO}_3^-$	2.07	1.71	1.21

^aReferences: From Lawrence Livermore National Laboratory (LLNL) thermo.com.V8.R6+ unless otherwise noted

^bCalculated using Van't Hoff approximation equation with data from thermo.com.V8.R6+

^cLumsdon and Farmer [1995]

^dCalculated using Van't Hoff approximation equation with $\Delta H_r = -96.8$ from Lumsdon and Farmer [1995]

throughout the hillslope for both R1 and R2 were utilized. This number is less than the total number of samples collected (n=915) because low sample volume precluded complete analysis for some samples. Only samples receiving complete analysis were included for input into SpecE8.

Since $\text{O}_{2(\text{aq})}$ was not measured directly, calculations were performed across a range of potential $\text{O}_{2(\text{aq})}$ concentrations between 0.1 mg L⁻¹ and 8 mg L⁻¹ to assess redox-sensitive mineral transformations. Dissolved O_2 (DO) concentrations impacted Mn-oxide SI values, driving otherwise higher magnitude SI values to lower values with a decrease in DO from 8 mg L⁻¹ to 0.1 mg L⁻¹. A concentration of 1 mg L⁻¹ was chosen for follow-on modeling as an intermediate value between that derived from equilibrium with atmospheric PO_2 (8 mg L⁻¹) and complete depletion of O_2 . This assumes modest $\text{O}_{2(\text{aq})}$ diffusion limitation.

The SI indicates the extent to which a particular solution is undersaturated or supersaturated with respect to a particular solid phase [Stumm and Morgan, 1996]:

$$SI = \log \Omega = \log \frac{Q}{K_{eq}} \quad (1)$$

where Q is the ion activity product derived from analytical data and aqueous phase speciation, and K_{eq} is the equilibrium constant for the mineral dissolution reaction. Positive values of SI values indicate supersaturation and precipitation of the solid phase, negative values indicate undersaturation and dissolution, and $SI = 0$ at equilibrium. Supersaturation of solutions was indicated with respect to approximately 68 mineral phases contained in the database (including those added by our team). Based on secondary minerals known to precipitate as a result of incipient basalt weathering [e.g., Chadwick and Chorover, 2001; Dontsova et al., 2009; Gislason et al., 1996; Stefansson and Gislason, 2001] we focused on the following 11 phases as potential products: birnessite, pyrolusite, proto-imogolite allophane, Mg-montmorillonite, heulandite, kaolinite, goethite, analcime, calcite, ferrihydrite and gibbsite. Full reactions and temperature-dependent dissolution equilibrium constants for these phases are given in Table 3.

Allophane (proto-imogolite form), an important secondary mineral phase formed during early stage basalt weathering [Stefansson and Gislason, 2001], was added to the thermo.dat database [Lumsdon and Farmer, 1995; Dobrzynski, 2006; Lawrence Livermore National Laboratory, LLNL database]. The Van't Hoff approximation was employed to solve for temperature dependence of $\log K_{SO}$ values:

$$\log K^t = \log K_{std}^t - \frac{\Delta H_{std}}{2.3025R} \left(\frac{1}{T} - \frac{1}{T_{std}} \right) \quad (2)$$

where ΔH_{std} is the standard enthalpy of reaction, R is the universal gas constant, T is temperature (K), T_{std} is the reference temperature, and K^t and K_{std}^t are the equilibrium constants at required and reference temperatures, respectively.

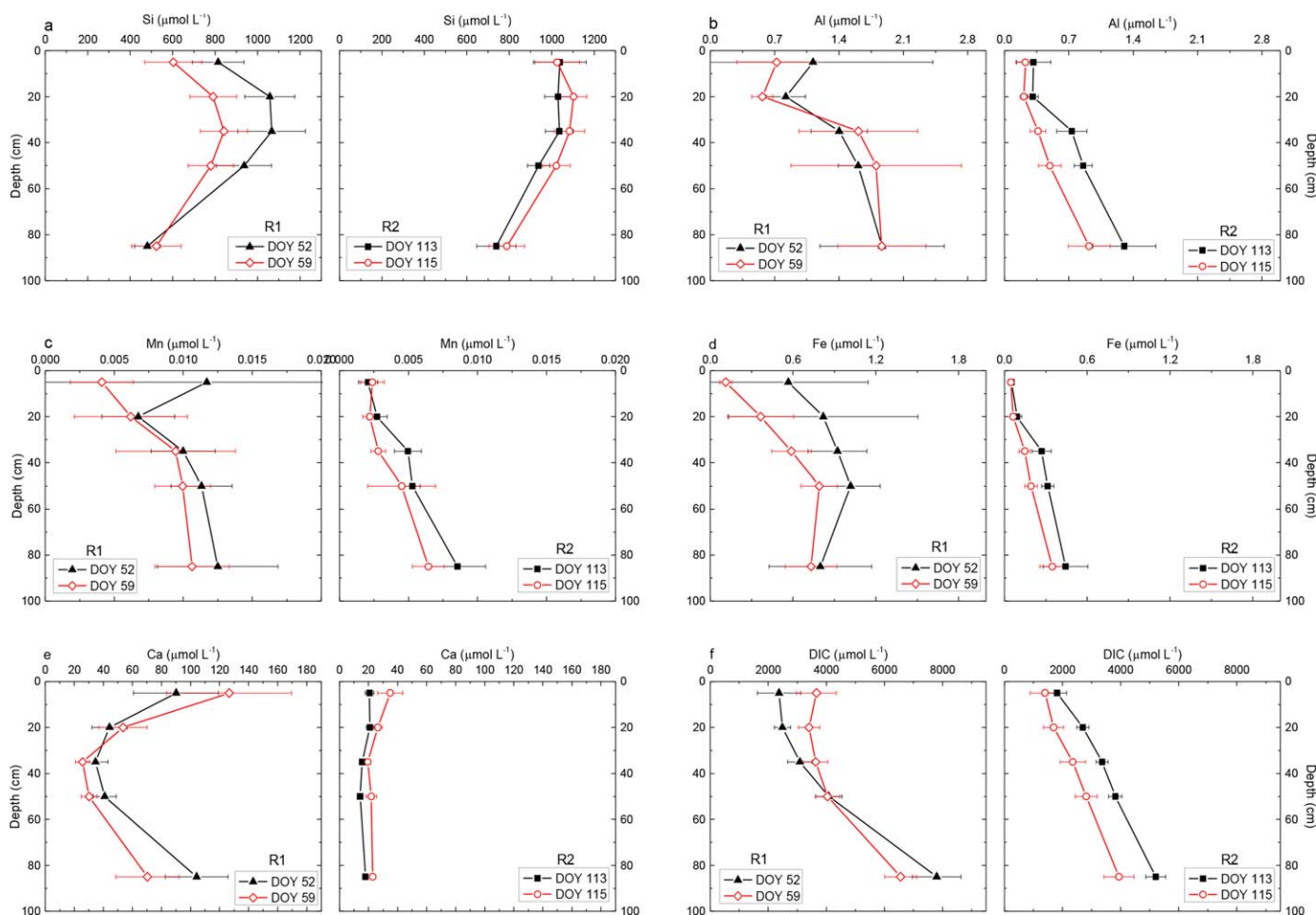


Figure 3. Depth profiles for means of constituent elements and DIC concentrations at 0.05, 0.2, 0.35, 0.55 and 0.85 m for R1 and R2. Error bars denote the 95% CI of the concentration means for each depth.

3. Results

3.1. Pore Water Chemistry

The pH values of pore waters collected throughout the hillslope were consistently alkaline (pH 8.5–9.5), indicating significant proton consumption upon contact of rainwater (pH 5.4) with basalt, consistent with proton-promoted silicate dissolution [Gislason *et al.*, 1996]. Dissolved Ca and dissolved inorganic carbon (DIC) concentration trends tracked closely over the days following R1 (ranging from 1 to 486 $\mu\text{mol L}^{-1}$ and 194 to 27,700 $\mu\text{mol L}^{-1}$, respectively) (see supporting information Figure S2). Aluminum concentrations generally declined over the course of drainage following R1, while comparison of concentrations for different sampler locations revealed no trend based on sampler location. Dissolved Al concentrations ranged from 0.1 to 27 $\mu\text{mol L}^{-1}$. Dissolved Si concentrations, ranging from 13 to 2190 $\mu\text{mol L}^{-1}$, were generally stable over time for the first 4 days of sampling (DOY 50–53), and then showed slight increases in concentration by DOY 59. Manganese concentrations, variable by sampler location, generally decreased with time, ranging from 0.01 to 0.22 $\mu\text{mol L}^{-1}$ overall. Iron concentrations also declined over the 10 day period of observed drainage, and showed no trends with respect to sampler location, ranging between 0.1 and 22 $\mu\text{mol L}^{-1}$.

Utilizing the whole-hillslope data sets from R1 and R2, sensor data and geochemical analyses were composited and averaged by depth to reveal depth-dependent trends (Figure 3 and supporting information Table S1). The 95% CI represents the large variation in chemistry within a given depth, which encompasses all hillslope regions shown in Figure 1. Pore water pH averaged 9.1 ± 0.04 following R1, and 8.6 ± 0.02 for R2. Temperature (T) was largely controlled by seasonal variation, and averaged $18^\circ \pm 0.15^\circ\text{C}$ following R1

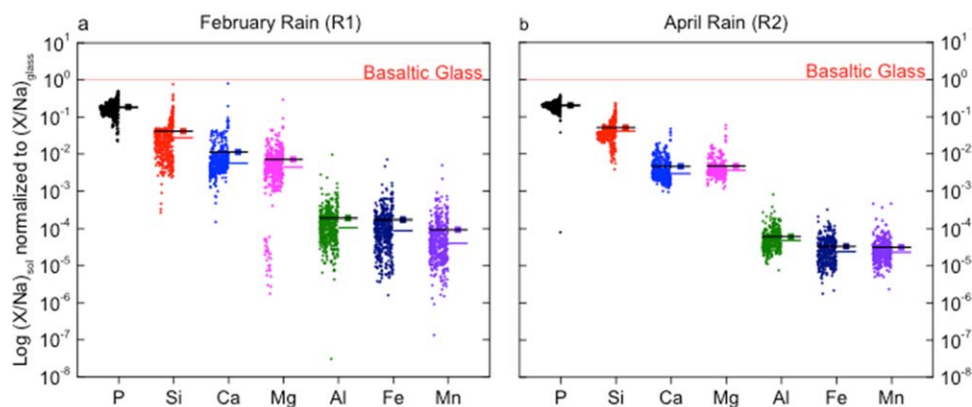


Figure 4. Pore water concentrations normalized to Na relative to corresponding molar ratios in the primary basaltic glass for R1 and R2. The horizontal red line represents congruent stoichiometric dissolution. Negative deviation from the line reflects the extent of preferential solid phase retention by some mechanism (e.g., secondary mineral formation, surface exchange, or nonstoichiometric dissolution). Each point represents an individual pore water sampler; lateral spread (left to right) of points is for visualization purposes only. Boxed line and straight line for each element represents mean and median, respectively.

(February), and $27 \pm 0.14^\circ\text{C}$ for R2 (April). Slight increases in T and pH were observed from the surface to the deeper depths (supporting information Table S1). Mean concentrations of Al, Mn, Fe, and DIC increased slightly with depth, whereas Si and Ca remained essentially unchanged or showed slight decreases (Figure 3). Overall, concentrations of Al, Mn, Fe, Ca, and DIC decreased from R1 to R2, whereas Si showed a slight increase.

The stoichiometry of major element (P, Si, Ca, Mg, Fe, Al, and Mn) dissolution was assessed by normalizing aqueous phase concentrations of rock-derived elements to those of Na over both R1 and R2 events. Sodium is selected as a mobile reference element because it exhibits the highest proportional release to pore waters of all lithogenic cations, it exhibits weak affinity for cation exchange sites, and its widespread precipitation from solution is not supported from thermodynamic modeling (only one Na-bearing secondary solid, Na-nontronite, an Fe^{III}-rich smectite was predicted to precipitate in selected cases from geochemical modeling). Aqueous element:Na concentration ratios were then normalized to the corresponding element:Na ratio in the primary glass (stoichiometry obtained by prior electron microprobe results, see *Pangle et al.* [2015]), and the results were plotted on a log scale to quantify the incongruity of basalt weathering (Figure 4). All cations exhibited negative deviation from the primary glass reference, i.e., target cations showed lower molar element:Na ratios in solution than in the glass (values less than unity in Figure 4), indicating nonstoichiometric release to mobile pore fluids. Apparent selective retention in solid-phase weathering products increased in the order $\text{P} < \text{Si} < \text{Ca} < \text{Mg} < \text{Al} < \text{Fe} < \text{Mn}$.

3.2. Thermodynamic Modeling

Aqueous phase speciation and saturation index (SI) values were calculated at the measured temperatures for all points in time and space for which the full requisite set of geochemical and sensor data were available ($n = 655$). Modeling results indicated that solutions were consistently (in time and space) undersaturated with respect to the primary minerals labradorite, forsterite, diopside and magnetite found in the basalt, with only a few instances of slight supersaturation ($1 < \text{SI} < 2$) with respect to labradorite. Conversely, SI values greater than 0 were consistently measured throughout the hillslope for all 11 target secondary minerals. Solutions showed reduced supersaturation ($\log \Omega < 2$) or undersaturation ($\log \Omega < 0$) with respect to four of the relatively soluble phases—calcite, ferrihydrite, gibbsite and analcime, depending on location (Table 4).

R2 showed lower supersaturation values than R1 for all phases except for the Fe (oxy)hydroxides (e.g., reflected in mean values, Tables 4 and 6). Highest SI values were consistently observed for the Mn oxides (birnessite and pyrolusite). $\text{SI}_{\text{birnessite}}$ values ranged from 21 to 55 for R1, and 30 to 50 for R2, while $\text{SI}_{\text{pyrolusite}}$ values ranged from 4 to 9.5 for R1 and 6 to 8.5 for R2. Pore solutions were also supersaturated with respect to secondary aluminosilicates throughout the hillslope and experiment. Proto-imogolite allophane and Mg-montmorillonite showed the highest SI values among the secondary aluminosilicates, and tracked together

Table 4. Mean Saturation Indices (log Ω) for Each Depth^a

	Depth (cm)	n	Birnessite	Pyrolusite	Proto-Imogolite	Montmorillonite	Heulandite	Kaolinite	Analcime	Gibbsite	Goethite	Ferrihydrite	Calcite
R1													
DOY	5	30	37(3) a	7.0(0.4) a	4.6(0.5) a	3.3(0.5) a	2.7(0.9) a	0.69(0.5) a	-0.53(0.4) a	-0.73(0.2) a	4.9(0.2) a	0.43(0.2) a	-0.12(0.3) a
52	20	44	42(1) b	7.6(0.2) b	4.7(0.3) a	3.7(0.3) a	3.2(0.5) a	0.83(0.4) a	0.09(0.2) b	-0.74(0.2) a	5.2(0.1) b	0.71(0.1) b	-0.03(0.2) a
	35	35	44(1) b,c	7.8(0.2) b,c	4.4(0.6) a	3.7(0.5) a	3.1(0.8) a	0.62(0.6) a	0.22(0.3) b,c	-0.82(0.3) a	5.3(0.1) b	0.88(0.1) b	0.05(0.2) a
	50	51	46(1) c	8.1(0.1) c	4.9(0.3) a	4.0(0.3) a	3.2(0.5) a	1.1(0.3) a	0.43(0.1) c	-0.55(0.1) a	5.5(0.1) b	1.0(0.1) b	0.12(0.1) a
	85	31	47(1) c	8.2(0.1) c,d	4.7(0.3) a	3.5(0.3) a	2.2(0.4) a	0.58(0.3) a	0.33(0.1) c	-0.61(0.1) a	5.2(0.2) b	0.74(0.2) a,b	0.74(0.1) b
DOY	5	13	40(3) a	7.4(0.4) a	5.1(0.6) a	3.7(0.5) a	2.9(0.8) a	1.2(0.6) a	-0.1(0.3) a	-0.49(0.3) a	4.6(0.2) a	0.14(0.2) a	0.26(0.3) a
59	20	29	41(2) b	7.5(0.3) a	4.7(0.3) a	3.6(0.3) a	2.8(0.6) a	0.90(0.4) a	0.01(0.2) a	-0.67(0.2) a	5.0(0.1) b	0.50(0.1) b	-0.05(0.2) a
	35	28	44(2) b,c	7.8(0.2) a,b	5.1(0.5) a	3.9(0.4) a	3.1(0.5) a	1.3(0.5) a	0.38(0.2) b	-0.49(0.2) a	5.2(0.1) c	0.79(0.1) c	-0.15(0.2) a
	50	44	46(1) c	8.1(0.1) b	5.3(0.4) a	3.6(0.6) a	2.7(1.1) a	1.4(0.5) a	0.31(0.3) b	-0.34(0.1) a	5.4(0.1) d	0.97(0.1) d	-0.15(0.1) a
	85	28	46(2) c	8.1(0.2) b,c	5.1(0.4) a	2.9(0.4) a	2.1(0.8) a	1.0(0.4) a	0.33(0.2) c	-0.37(0.2) a	5.3(0.1) c,d	0.87(0.1) c,d	0.43(0.2) b
R2													
DOY	5	20	36(1) a	6.9(0.1) a	2.9(0.4) a	2.3(0.4) a	0.9(0.5) a	-0.51(0.5) a	-1.1(0.3) a	-1.4(0.2) a	3.9(0.1) a	-0.46(0.1) a	-0.75(0.1) a
113	20	38	38(1) b	7.1(0.1) b	3.2(0.2) a	2.6(0.2) a	1.4(0.2) a	-0.22(0.2) b	-0.68(0.1) b	-1.2(0.1) a	4.2(0.1) b	-0.18(0.1) b	-0.53(0.1) b
	35	32	41(1) c	7.5(0.1) c	4.0(0.2) b	3.3(0.2) b	2.1(0.2) a	0.57(0.2) c	-0.16(0.1) c	-0.86(0.1) b	4.7(0.1) c	0.35(0.1) c	-0.56(0.1) b
	50	46	42(1) c	7.6(0.1) c,d	4.2(0.2) b	3.4(0.1) b	2.1(0.2) a	0.75(0.2) c	-0.05(0.1) c	-0.75(0.1) b	4.8(0.1) c	0.47(0.1) c	-0.57(0.1) b
	85	30	44(1) d	7.8(0.1) d	4.4(0.2) b	3.3(0.2) b	1.8(0.4) a	0.76(0.2) c	0.09(0.1) c,d	-0.64(0.1) b	4.9(0.1) c	0.53(0.1) c	-0.30(0.1) c
DOY	5	15	38(1) a	7.0(0.1) a	2.9(0.4) a	2.4(0.3) a	1.2(0.4) a	-0.56(0.4) a	-1.0(0.2) a	-1.4(0.2) a	3.9(0.2) a	-0.49(0.2) a	-0.49(0.1) a
115	20	39	38(1) a	7.1(0.1) a	3.3(0.2) a	2.8(0.2) a	1.7(0.2) a	-0.11(0.2) a	-0.72(0.1) b	-1.3(0.1) a	4.1(0.1) b	-0.24(0.1) b	-0.55(0.1) a
	35	33	40(1) b	7.3(0.1) b	3.6(0.2) a,b	3.0(0.2) a,b	2.0(0.3) a	0.16(0.2) a,b	-0.36(0.1) c	-1.1(0.1) a	4.5(0.1) c	0.11(0.1) c	-0.49(0.1) a
	50	43	41(1) b,c	7.4(0.1) b	3.7(0.2) b	3.1(0.1) b	1.9(0.2) a	0.31(0.2) b	-0.29(0.1) c,d	1.0(0.1) b	4.6(0.1) c	0.23(0.1) c	-0.47(0.0) a
	85	29	43(1) c	7.7(0.1) c	4.4(0.2) b	3.4(0.2) b	2.0(0.4) a	0.81(0.2) c	0.07(0.1) d	-0.67(0.1) c	4.9(0.1) d	0.50(0.1) c	-0.30(0.1) b

^aError in parentheses presented as 95% confidence interval for each depth mean. a, b, c, d and e represent statistically significant differences with depth where 95% confidence intervals did not overlap.

in time and space, ranging between 2 and 8.5 for R1 and 1 to 6 for R2. It should be noted that there were some instances of undersaturation with respect to Mg-montmorillonite on DOY 59 following R1. SI values for Fe (oxy)hydroxides (goethite and ferrihydrite) did not change significantly between the two rain events, and they ranged from 3 to 6 and -1 to 2 for goethite and ferrihydrite, respectively. Undersaturation of ferrihydrite was largely restricted to the central trough region (Table 6). Solutions were undersaturated with respect to Al hydroxide (gibbsite) for much of the experiment, with SI values ranging from -2 to 1 for R1 and -2 to 0.4 for R2 (Tables 4 and 6).

SI values of solutions specific to the minerals of interest were also averaged and examined for depth dependence (Table 4). Following R1, significant depth dependency in SI values was observed for birnessite, pyrolusite, analcime, goethite, ferrihydrite and calcite. However, SI values for proto-imogolite allophane, montmorillonite, heulandite, kaolinite and gibbsite showed no significant depth dependence. Following R2, all mineral phases except heulandite exhibited significant mean SI variation with depth. Solution phase undersaturation was exhibited in surface depths for analcime and calcite following R1 and for ferrihydrite following R2. When examined as means by depth, solutions were undersaturated with respect to calcite for all depths following R2, while solutions were undersaturated with respect to gibbsite for all depths following both R1 and R2. In general, SI value means were higher for R1 relative to R2.

3.3. Variation by Topographic Region

Since topography influences the movement of water through a basin [Tetzlaff et al., 2009], distinct topographic regions within the hillslope were grouped in data analysis to assess whether pore water in those locations exhibited distinctive aqueous geochemical signatures. These regions for LEO east - defined as upslope, inner shoulder, outer shoulder and central trough (Figure 1) - represent areas with distinct hydrologic behaviors during the rainfall events. During R1 and R2, the upslope region exhibited a prevalence of unsaturated flow dominated by vertical infiltration. As a result, it was subject to less lateral inflow from neighboring regions, and shorter durations of saturated flow relative to the central trough region. The latter was subject to more substantial lateral inputs and much longer durations of saturation [Gevaert et al., 2014]. Therefore, to complement the depth-dependent trend analysis, we averaged and compared the geochemistry and SI value data from different topographic regions of the hillslope (Tables 5 and 6).

While trends are suggested by mean values, only DIC, Mg, Ca and Mn concentrations displayed statistically significant differences between the upslope and central trough regions (Table 5). Among these, all except

Table 5. Means for Each Region^a

Region	n	VWC (%)	pH -Log(H ⁺)	DIC (μmol L ⁻¹)	Na (μmol L ⁻¹)	Mg (μmol L ⁻¹)	Al (μmol L ⁻¹)	Si (μmol L ⁻¹)	P (μmol L ⁻¹)	Ca (μmol L ⁻¹)	Mn (μmol L ⁻¹)	Fe (μmol L ⁻¹)	
<i>R1</i>													
DOY 52	Upslope	24	22(5)	9.0(0.2)	3320(814)	3473(883)	14(6) -	1.8(0.3)	1400(199)	79(24)	27(6) -	0.01(0.003) +	0.84(0.2)
	Outer Shoulder	48	26(4)	9.2(0.1)	4518(812)	4478(979)	32(13)	1.5(0.5)	1177(158)	86(17)	43(12)	0.01(0.004)	0.89(0.3)
	Inner Shoulder	79	28(3)	9.1(0.1)	3805(608)	4221(779)	31(10)	1.5(0.7)	940(94)	76(17)	48(10)	0.01(0.006)	1.1(0.6)
	Central Trough	84	28(3)	9.2(0.1)	3766(540)	4486(688)	47(11) +	0.88(0.2)	576(53)	80(12)	86(18) +	0.01(0.002) -	0.57(0.2)
DOY 59	Upslope	12	12(2)	8.7(0.2)	3670(752)	4375(907)	13(8)	1.1(0.3)	870(150)	114(24)	27(11) -	0.004(0.002)	0.61(0.2)
	Outer Shoulder	26	14(2)	9.0(0.1)	5387(770)	5483(1044)	28(14)	1.2(0.4)	636(153)	152(28)	57(26)	0.01(0.0003)	0.57(0.2)
	Inner Shoulder	57	15(1)	9.0(0.1)	3857(388)	4227(450)	17(4)	1.7(0.4)	770(92)	111(15)	35(7)	0.01(0.003)	0.77(0.1)
	Central Trough	75	13(1)	8.9(0.1)	4286(400)	4557(473)	26(6)	1.0(0.3)	1133(80)	109(14)	71(13) +	0.01(0.002)	0.42(0.1)
<i>R2</i>													
DOY 113	Upslope	27	18(2)	8.7(0.1)	3661(390) +	3616(425)	13(1) -	0.91(0.4)	1133(79)	81(13)	14(1)	0.01(0.002)	0.37(0.2)
	Outer Shoulder	32	20(3)	8.6(0.1)	4590(600)	4552(688)	19(4)	0.69(0.2)	1088(91)	94(18)	20(2)	0.01(0.001)	0.23(0.1)
	Inner Shoulder	60	20(2)	8.6(0.1)	399(291)	3936(389)	16(2)	0.72(0.1)	999(68)	84(10)	18(1)	0.005(0.001)	0.27(0.1)
	Central Trough	82	19(1)	8.7(0.0)	2937(196) -	3497(432)	16(2) +	0.62(0.1)	844(46)	81(9)	18(2)	0.004(0.001)	0.18(0.0)
DOY 115	Upslope	25	16(2)	8.6(0.1)	3362(722)	3012(391)	13(3) -	0.38(0.1)	1128(113)	84(14)	21(5)	0.004(0.001)	0.16(0.1)
	Outer Shoulder	36	16(2)	8.6(0.0)	3768(688)	4125(679)	21(4)	0.49(0.1)	1142(85)	101(18)	26(3)	0.01(0.004)	0.18(0.1)
	Inner Shoulder	62	18(2)	8.6(0.0)	3422(390)	3728(359)	16(2)	0.46(0.1)	1030(55)	88(11)	21(1)	0.004(0.001)	0.19(0.0)
	Central Trough	80	16(1)	8.6(0.0)	2668(238)	3296(361)	19(2) +	0.41(0.1)	913(50)	81(10)	26(4)	0.003(0.001)	0.13(0.0)

^aError in parentheses presented as 95% confidence interval for each depth mean. + and - denotes high and low concentrations, respectively, comparing upslope and central trough regions. When marked, 95% confidence intervals do not overlap.

DIC showed higher concentrations in the central trough relative to the upslope region. DIC showed the opposite trend – higher upslope concentrations relative to central trough. These spatial trends were variable in time, and sometimes occurred on only one of the sampling days following R1 or R2. For instance, Mn only showed greater concentration in the central trough relative to the upslope region on DOY 52 following R1.

Mean SI values were also examined for statistically significant regional trends. SI values were greater in the upslope regions relative to the central trough for all mineral phases except calcite, which showed the opposite trend (greater SI means in the central trough relative to upslope) (Table 6). Unlike R1, during R2, allophane, gibbsite and calcite did not exhibit any statistically significant region-specific differences. Further, those phases for which higher SI values were observed in the upslope region relative to the central trough did so only on sampling DOY 113.

Table 6. Mean Saturation Indices (log Ω) for Each Region^a

Region	n	Proto-Birnessite	Pyrolusite	Imogolite	Montmorillonite	Heulandite	Kaolinite	Analcime	Gibbsite	Goethite	Ferrihydrite	Calcite	
<i>R1</i>													
DOY 52	Upslope	13	47(1) +	8.2(0.2) +	5.8(0.4) +	5.1(0.4) +	4.7(0.8) +	2.2(0.5) +	0.79(0.2) +	-0.21(0.2) +	5.5(0.1) +	1.1(0.1) +	-0.27(0.3) -
	Outer Should	31	46(1)	8.1(0.1)	4.9(0.2)	4.2(0.3)	3.6(0.6)	1.1(0.3)	0.48(0.2)	-0.63(0.1)	5.3(0.1)	0.87(0.1)	0.13(0.2)
	Inner Should	60	44(1)	7.8(0.2)	4.9(0.2)	3.9(0.3)	3.3(0.4)	1.0(0.3)	0.31(0.1)	-0.61(0.1)	5.3(0.1)	0.87(0.1)	0.08(0.1)
	Central Trough	83	41(1) -	7.5(0.2) -	4.2(0.3) -	3.0(0.3) -	2.0(0.4) -	0.23(0.4) -	-0.22(0.2) -	-0.86(0.2) -	5.1(0.1) -	0.62(0.1) -	0.28(0.1) +
DOY 59	Upslope	8	45(1) +	8.0(0.2) +	5.6(0.4) +	4.3(0.3) +	4.5(1.6) +	1.9(0.3) +	0.89(0.5) +	-0.23(0.2) +	5.5(0.1) +	1.0(0.1) +	-0.34(0.3) -
	Outer Should	18	45(2)	8.0(0.2)	4.9(0.3)	3.3(0.5)	2.5(0.9)	1.0(0.4)	0.3(0.2)	-0.51(0.1)	5.3(0.1)	0.81(0.1)	0.21(0.2)
	Inner Should	41	45(1)	8.0(0.2)	5.5(0.3)	4.1(0.3)	3.6(0.6)	1.7(0.3)	0.60(0.2)	-0.29(0.1)	5.4(0.1)	0.97(0.1)	-0.15(0.1)
	Central Trough	73	42(1) -	7.7(0.2) -	4.7(0.3) -	3.2(0.4) -	2.1(0.6) -	0.78(0.3) -	-0.04(0.2) -	-0.59(0.1) -	5.0(0.1) -	0.55(0.1) -	0.12(0.1) +
<i>R2</i>													
DOY 113	Upslope	15	42(1) +	7.70(2) +	4.0(0.3)	3.5(0.3) +	2.4(0.6) +	0.68(0.3) +	-0.03(0.4) +	-0.86(0.2)	4.8(0.2) +	0.41(0.2) +	-0.50(0.1)
	Outer Should	19	42(1)	7.5(0.1)	4.2(0.2)	3.5(0.2)	2.3(0.3)	0.78(0.2)	-0.01(0.2)	-0.76(0.1)	4.7(0.1)	0.34(0.1)	-0.47(0.1)
	Inner Should	50	41(1)	7.5(0.1)	4.0(0.2)	3.3(0.1)	2.0(0.2)	0.61(0.2)	-0.15(0.1)	-0.83(0.1)	4.7(0.1)	0.37(0.1)	-0.47(0.1)
	Central Trough	80	40(1) -	7.3(0.1) -	3.5(0.2)	2.7(0.2) -	1.3(0.2) -	0.04(0.2) -	-0.55(0.1) -	-1.1(0.1)	4.4(0.1) -	0.03(0.1) -	-0.57(0.1)
DOY 115	Upslope	12	40(1)	7.3(0.2)	3.7(0.3)	3.0(0.3)	1.9(0.6)	0.27(0.3)	-0.43(0.3)	-1.0(0.1)	4.5(0.2)	0.12(0.2)	-0.46(0.1)
	Outer Should	21	41(1)	7.5(0.1)	3.8(0.2)	3.2(0.2)	2.1(0.3)	0.36(0.2)	-0.26(0.2)	-1.0(0.1)	4.5(0.1)	0.11(0.1)	-0.39(0.1)
	Inner Should	51	41(1)	7.4(0.1)	3.8(0.2)	3.2(0.1)	2.1(0.2)	0.37(0.2)	-0.23(0.1)	-0.99(0.1)	4.6(0.1)	0.24(0.1)	-0.45(0.1)
	Central Trough	75	39(1)	7.2(0.1)	3.5(0.2)	2.8(0.2)	1.6(0.2)	0.00(0.2)	-0.58(0.1)	-1.1(0.1)	4.3(0.1)	-0.06(0.1)	-0.50(0.1)

^aError in parentheses presented as 95% confidence interval for each regional mean. + and - denotes high and low SI values, respectively, comparing upslope and central trough regions. When marked, 95% confidence intervals do not overlap.

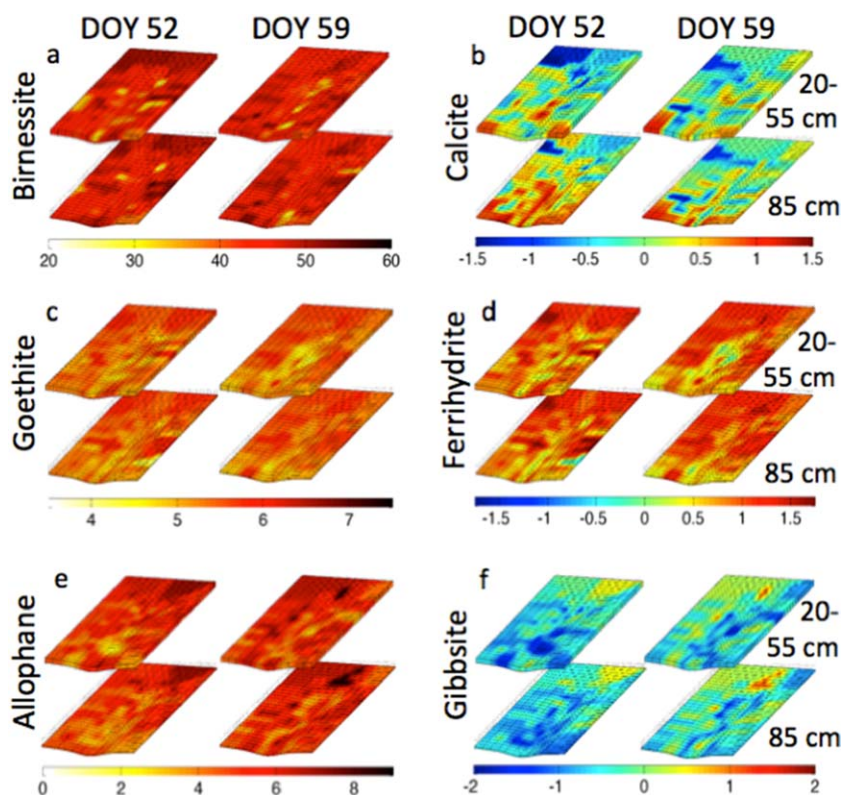


Figure 5. Three-dimensional interpolations of saturation index rendered onto the hillslope schematic at two depth intervals (20–55 cm and ≥ 85 cm) and two sampling dates (DOY 52 and DOY 59) for six secondary minerals. Warm colors (dark in BW) represent areas of supersaturation while cool colors (light in BW) represent areas of reduced supersaturation or undersaturation. Note each mineral type has a unique scale for saturation index (i.e., $\log Q/K$).

3.4. Spatial Interpolation of Geochemistry Data

The SI values for secondary phases were interpolated to reveal spatial variation at the hillslope scale using a Matlab 3D code (Figure 5). The program optimized interpolation based on a nearest-neighbor weighted approach in which sample locations with results are incorporated into estimates of the values for locations lacking sample coverage. Interpolations show spatial patterns for secondary mineral SI values at various depths and over a one-week period following R1. These results support the regional mean SI value analysis (Table 6), illustrating higher mean values in the upslope region relative to the central trough (Figures 5a, 5c, 5d, 5e, and 5f). The unique trend for calcite, with higher SI values in the central trough relative to the upslope region is also well visualized with the 3-D plots (Figure 5b). The undersaturation of solutions with respect to gibbsite (Figure 5f) and supersaturation of solutions with respect to Al-containing allophane (Figure 5e) is clear.

3.5. Colloidal Transport

Widespread supersaturation of solution with respect to colloid-forming phases (e.g., Figure 5) raised the question of potential nanoparticle transport in hillslope porewaters. However, the presence of only small amounts of colloidal material (110–2000 nm) in pore water sampler solutions were indicated, and only for those elements plotting above the 1:1 line in Figure 6. Regressions for the majority of analyzed elements, including Si (Figure 6b), Ca, Mg, Mn and others (data not shown) are statistically identical to the 1:1 line. However, regression lines for Al, P and Fe (Figures 6a, 6c and 6d, respectively) showed statistically significant positive deviation from the 1:1 line, either as a regression slope greater than 1.0 (Al, Fe) or an intercept greater than zero (P). None of the other elements analyzed indicated significant colloidal influence.

4. Discussion

Results presented here are consistent with rapid dissolution of a glass-dominated basalt coupled to neoformation of poorly to moderately crystalline secondary phases, with transformations occurring over even

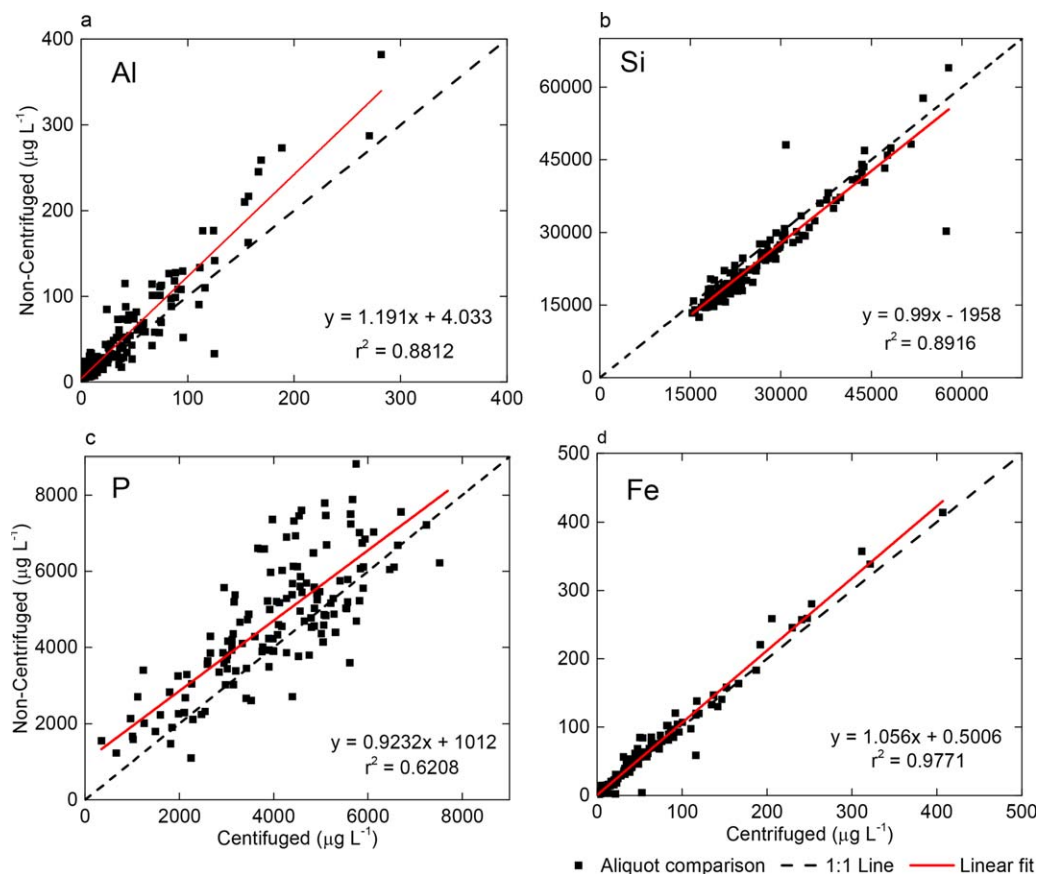


Figure 6. Comparison of concentrations for Al, Si, Fe and P in centrifuged and noncentrifuged pore water samples to quantify colloidal material in the 110–2000 nm size range. Results of linear regressions are shown by solid red lines, whereas the 1:1 line is shown as dashed black line. Regressions with slope significantly greater than 1.0 or y-intercept significantly greater than zero (beyond 95% confidence interval) reveal colloid sized material (a, c, and d). Samples plotting close to the 1:1 line (where centrifuged equal noncentrifuged concentrations) indicate a lack of colloidal material for that element (e.g., Si).

relatively short water-rock interaction times. Given that the study was conducted with freshly ground basalt, the observed initial weathering reactions and SI values could potentially reflect the fastest transformation rates that will be observed over the LEO lifetime. This is because for a given phase, mass normalized dissolution rates are greater for smaller particles because of their higher specific surface area [Zhang *et al.*, 1993]. Furthermore, grinding of the basalt prior to emplacement in the hillslopes undoubtedly resulted in an increased prevalence of fresh surfaces that are more susceptible to ion hydration and mobilization than surfaces exposed to prior water reaction wherein a leached layer may occur that slows dissolution rate [Oelkers, 2001]. Indeed, the data do suggest a slight decrease in silicate dissolution rate even between R1 and R2.

Modeling conducted by Dontsova *et al.* [2009] concluded basalt glass would undergo the most rapid dissolution followed by forsterite (a Mg-rich olivine). Furthermore, Dontsova *et al.* [2009] showed that crystalline basaltic minerals were embedded within the glass matrix, implying that glass dissolution would need to proceed prior to hydration of crystalline silicates. The incipient preferential weathering of glass is also supported by previous weathering studies of basalt silicate rock [Oelkers and Gislason, 2001; Gislason and Oelkers, 2003].

4.1. Weathering Incongruency

The molar metal(loid) to Na ratio in pore water normalized to the same in the basaltic glass provides a reference for congruency of dissolution. Whereas the red line in Figure 4 represents congruent glass dissolution, observed deviation from stoichiometric dissolution (unity) to lower values on the log scale indicates preferential removal from solution of Si, Ca, Mg, Al, Fe, Mn and P via secondary phase precipitation, adsorption,

nonstoichiometric glass dissolution, or some combination thereof. Geochemical modeling results suggest that deviations from stoichiometric release are the result of preferential re-precipitation in the order of $Mn \geq Fe \sim Al \gg Mg > Ca > Si > P$ in secondary solids. Prior work also indicates Al, Fe and Mn are among the least mobile elements during oxic basalt weathering [Gislason *et al.*, 1996; Nesbitt and Wilson, 1992; Stefansson and Gislason, 2001]. Modeling results (Figure 5; Tables 4 and 6) suggest that solid phase retention of Fe is principally in neo-formed ferric (oxy)hydroxides (e.g., goethite and ferrihydrite). Conversely, several potential secondary minerals may be contributing to solid phase retention of Al, since solutions exhibit saturation states with respect to potentially forming solids that extend from near equilibrium (e.g., gibbsite) to highly supersaturated (e.g., allophane, kaolinite, montmorillonite) (Figure 5; supporting information Figure S2; Tables 4 and 6). Neoformation of aluminosilicates would also explain the solid phase retention of Si observed in these experiments.

An important finding of the R1 and R2 experiments was that incipient dissolution of the granular basalt is sufficiently rapid such that within hours to days of rainfall, pore waters become equilibrium-saturated to highly supersaturated with respect to a wide range of secondary solids, including those that are known to exhibit rapid precipitation kinetics at low temperature, low pressure, Earth surface conditions (e.g., allophane, ferrihydrite). According to the Ostwald Step Rule, formation of more soluble phases, such as ferrihydrite, allophane, or poorly crystalline gibbsite may be favored initially, because these solids have a lower interfacial energy and hence lower activation barriers to nucleation [Stumm and Morgan, 1996]. Ostwald ripening includes the conversion of these higher solubility, poorly-crystalline solids to less soluble, more crystalline solids (e.g., goethite, kaolinite) over longer reaction times, as pore water concentrations of mineral elements in equilibrium with these solids decreases [Steefel and van Cappellen, 1990]. Hence, our geochemical modeling of LEO porewaters suggests that the secondary solids forming during the initial R1 and R2 events are likely to be poorly-crystalline minerals including ferrihydrite and allophane. Destructive solid phase analyses were avoided in these early stages of hillslope weathering, but will be conducted at a later time.

Whereas there was no indication of supersaturation of solutions with respect to phosphate minerals, P was nonetheless preferentially retained in the solid phase by an order of magnitude relative to what would be expected assuming stoichiometric release. These observations are consistent with the high affinity of the phosphate oxyanion for surface functional groups of hydroxylated minerals that are likely to form, such as ferrihydrite, allophane and gibbsite under the range of LEO temperature (17–27°C) and pH conditions (8.5–9.5) [Goldberg and Sposito, 1984a; Parfitt, 1989; van Emmerik *et al.*, 2007].

Adsorption to both primary and secondary mineral surfaces could also account for the removal of Ca and Mg from solution (Figure 4), given their greater affinity for surface binding sites relative to monovalent cations. Adsorption to the surface of allophane (negatively charged at the pH of LEO porewaters), interlayer adsorption to aluminosilicate clays such as smectite, and precipitation as calcite or Mg-calcite likely also played a role in removal of these cations from solution.

Manganese showed the largest net retention relative to Na (Figure 4), with a net release to solution 4–5 orders of magnitude lower than would be predicted on the basis of stoichiometric dissolution of the basaltic glass reference. Solutions were supersaturated with respect to Mn oxides, birnessite and pyrolusite, for all samples collected in this study. Indeed, SI for birnessite was highest of all modeled phases. In contrast to other alteration products and surface interactions, birnessite formation is limited kinetically in the absence of microbial catalysis under LEO temperature and pH [Tebo *et al.*, 2004]. Apparently, microbial activity in the oligotrophic environment of LEO basalt may play an important role in secondary Mn phase formation.

4.2. Hillslope Scale Patterns of Geochemical Saturation

We had hypothesized that pore water supersaturation values would increase with distance along flowpaths, leading to down-gradient deposition of neo-formed solids. However, long water-rock contact times along flowpaths were evidently not required and supersaturated solutions were observed relatively uniformly throughout the hillslope (Figures 5a, 5c, 5d, and 5e). Water flux and reaction kinetics govern the length of flowpaths from source to sink for reaction products, and the incipient production of secondary, tertiary, etc., minerals in this system should continue until constituent concentrations become limiting [Chadwick and Chorover, 2001].

While it is the case that pore waters were supersaturated with respect to secondary minerals throughout the hillslope following R1 and R2, there is an apparent trend toward lower SI values in the central trough relative to upslope regions except in the case of calcite (Table 6 and Figure 5). One interpretation of this patterning (for all except calcite) is that secondary precipitates are formed dominantly during vertical infiltration of solution in upslope regions, and solutions comprising lower solute concentrations make their way into the central trough. Another is that the trough itself is becoming enriched in neo-formed precipitates whose surfaces are favorable for further crystal growth of secondary minerals, thereby reducing pore water concentrations and SI values of percolating solutions. Indeed, distinguishing the precise locations of secondary precipitate accumulations will require core sampling to be conducted at a later time. Reactive transport (CrunchFlow) modeling performed for LEO hillslope during the design stage predicted precipitation of secondary minerals in the unsaturated zone in upslope regions and not in the trough [Dontsova *et al.*, 2009], therefore supporting the 1st hypothesis. The contrasting upslope versus central trough regional averages for SI values, and the lower concentrations and associated lower SI values in the central trough for the 3-D plots following R1 point to a strong likelihood of secondary mineral formation in central trough region. The second rain event (R2), with markedly less water input, showed less regional variation for most elemental concentrations and thus less variation in the modeled mineral saturation. Both the 3-D interpolation plots (Figure 5) and regional averages (Table 6) of SI values for all target minerals except calcite indicated diminished supersaturation toward equilibrium, or a reduction from near equilibrium to undersaturated values in the central trough relative to the upslope region.

In contrast, to the pattern of lower SI values in the central trough relative to upslope for aluminosilicates and metal oxides (Figures 6a, 6c, 6d, 6e, and 6f), for calcite the highest SI values occurred in the central trough (Figure 6b). This effect appears driven by accumulation of higher pore water Ca concentrations in the central trough relative to upslope, particularly during R1 (Table 5). Given that upgradient pore water was consistently undersaturated with respect to calcite, the behavior of SI_{calcite} is, in effect, more consistent with our initial hypothesis of solute accumulation to saturation thresholds along the flow path.

4.3. Neof ormation of Mobile Colloids

The initial survey of samples taken following R1 provided direct evidence of colloid-sized material mobilized into pore water from all topographic regions and depths of the LEO hillslope. Aluminum, P and Fe each showed significantly higher concentrations in noncentrifuged relative to centrifuged aliquots (Figure 3) indicating that these elements are represented in the mobile colloidal (110–2000 nm) pool. Despite this fact, colloidal contributions are small relative to totals or truly dissolved fractions.

The predominance of the truly dissolved fraction for other elements suggests that the provenance of colloidal Al, P, and Fe is nucleation and growth of secondary minerals from supersaturated pore waters. Under the high pH (pH ~9) and oxic conditions of LEO porewaters, Fe^{II} released from primary silicate weathering rapidly oxidizes to Fe^{III} and hydrolyzes to form Fe (oxy)hydroxides of low solubility [Cornell and Schwertmann, 2003]. Likewise, Al hydrolysis and either coprecipitation with Si to form allophane or precipitation as gibbsite, could explain the colloidal contributions of Al. As discussed above, geochemical modeling of pore waters indicated widespread supersaturation with respect to ferrihydrite, goethite, and, to a lesser extent, gibbsite, all of which are known to be high affinity adsorbents for phosphate P [Goldberg and Sposito, 1984a; Parfitt, 1989; van Emmerik *et al.*, 2007], which is consistent with colloidal forms of that element. It is important to note that the lack of evidence supporting a mobile colloidal fraction for Si (Figure 6) could be the result of extremely high Si concentrations such that any evidence for colloidal Si forms is hidden by analytical error (i.e., colloidal contributions are negligible relative to the dissolved pool).

5. Conclusions

Geochemical analyses and thermodynamic modeling of pore water chemistry during initial rain events on a model hillslope comprising a freshly ground basalt were consistent with rapid dissolution of basaltic glass and widespread supersaturation with respect to secondary aluminosilicates and metal oxides. Neo-phases comprising Al, P and Fe included a fraction that was present as mobile colloids, and potentially contributed to particulate matter (in addition to the more prevalent solute) redistribution in the hillslope. Early-stage spatial dependence was also indicated for solid phase weathering products.

While we initially hypothesized that dissolution would lead to development of progressive accumulation of solutes along flowpaths favoring precipitation of secondary phases down gradient, this was not clearly observed except in the case of calcite. Rather, supersaturation of solutions with respect to multiple other secondary minerals (e.g., aluminosilicates, metal (oxy)hydroxides), and formation of mobile Al, Fe and P bearing colloids was indicated for most topographic regions and depths. This patterning is consistent with high rates of mineral transformation giving rise to supersaturation over short water flow path lengths, which might be uniquely characteristic of this early weathering stage. Nevertheless, the development of depth dependence for some aluminosilicates and gibbsite following R2 (where none existed following R1), suggests that more pronounced spatial heterogeneity may be expected from continued irrigation of the LEO basalt. Surface coating of primary basalt by neo-formed secondary phases is expected to slow dissolution rates requiring longer water-rock contact time (i.e., longer flowpath length) to achieve comparable supersaturation as observed here over short distances.

Acknowledgments

This research was supported by the National Science Foundation, grant EAR-1417097. Data generated in support of this study are maintained in the Biosphere 2 database and are available upon request made to the corresponding author. The Biosphere 2 facility and the capital required to conceive and construct LEO were provided through a charitable donation from the Phileology Foundation, and its founder, Edward Bass. Gratitude is expressed to the Thomas R. Brown Foundations for support. Many thanks also to Mary Kay Amistadi in the Arizona Laboratory for Emerging Contaminants and Edward Hunt, Biosphere 2 Biogeochemistry Laboratory, for assistance with aqueous geochemical analyses.

References

- Barrett, E. P., L. G. Joyner, and P. P. Halenda (1951), The determination of pore volume and area distributions in porous substances. I. Computations from nitrogen isotherms, *J. Am. Chem. Soc.*, *73*, 373–380.
- Benedetti, M. F., et al. (2003), Chemical weathering of basaltic lava flows undergoing extreme climatic conditions: The water geochemistry record, *Chem. Geol.*, *201*(1–2), 1–17, doi:10.1016/S0009-2541(03)00231-6.
- Berner, R. A., A. C. Lasaga, and R. M. Garrels (1983), The carbonate-silicate geochemical cycle and its effect on atmospheric carbon-dioxide over the past 100 million years, *Am. J. Sci.*, *283*(7), 641–683.
- Bethke, C. M. (2011), *Biogeochemical Reaction Modeling*, 390 pp., Oxford Univ. Press, N. Y.
- Bluth, G. J. S., and L.R. Kump. (1994), Lithologic and climatologic controls of river chemistry, *Geochim. Cosmochim. Acta*, *58*(10), 2341–2359, doi:10.1016/0016-7037(94)90015-9.
- Brantley, S. L., et al. (2006), *Frontiers in Exploration of the Critical Zone: Report of a Workshop Sponsored by the National Science Foundation (NSF) October 24–26, 2005*, 30 pp., Newark, Delaware.
- Bronick, C. J., and R. Lal (2005), Soil structure and management: A review, *Geoderma*, *124*(1–2), 3–22.
- Chadwick, O. A., and J. Chorover (2001), The chemistry of pedogenic thresholds, *Geoderma*, *100*(3–4), 321–353, doi:10.1016/S0016-7061(01)00027-1.
- Chorover, J., M. K. Amistadi, and O. A. Chadwick (2004), Surface charge evolution of mineral-organic complexes during pedogenesis in Hawaiian basalt, *Geochim. Cosmochim. Acta*, *68*(23), 4859–4876, doi:10.1016/j.gca.2004.06.005.
- Chorover, J., R. Kretzschmar, F. Garcia-Pichel, and D. L. Sparks (2007), Soil biogeochemical processes within the critical zone, *Elements*, *3*(5), 321–326, doi:10.2113/gselements.3.5.321.
- Christensen, B. T. (2001), Physical fractionation of soil and structural and functional complexity in organic matter turnover, *Eur. J. Soil Sci.*, *52*(3), 345–353, doi:10.1046/j.1365-2389.2001.00417.x.
- Cornell, R. M., and U. Schwertmann (2003), *The Iron Oxides: Structure, Properties, Reactions, Occurrences, and Uses*, Wiley-VCH, Weinheim, Germany.
- Dessert, C., B. Dupré, J. Gaillardet, L. M. Francois, and C. J. Allègre (2003), Basalt weathering laws and the impact of basalt weathering on the global carbon cycle, *Chem. Geol.*, *202*(3–4), 257–273, doi:10.1016/j.chemgeo.2002.10.001.
- Dobrzynski, D. (2006), Silica solubility in groundwater from Permian volcanogenic rocks (the Sudetes Mts., SW Poland)—The role of reversible aluminosilicate solids, *Geol. Q.*, *50*(4), 407–417.
- Dontsova, K., C. I. Steefel, S. Desilets, A. Thompson, and J. Chorover (2009), Solid phase evolution in the Biosphere 2 hillslope experiment as predicted by modeling of hydrologic and geochemical fluxes, *Hydrol. Earth Syst. Sci.*, *13*(12), 2273–2286.
- Dontsova, K. D., Zaharescu, W. Henderson, S. Verghese, N. Perdrial, E. Hunt, and J. Chorover (2014), Impact of Organic Carbon on Weathering and Chemical Denudation of Granular Basalt, *Geochim. Cosmochim. Acta*, *139*, 508–526, doi:10.1016/j.gca.2014.05.010.
- Duffield, W., N. Riggs, D. Kaufman, D. Champion, C. Fenton, S. Forman, W. McIntosh, R. Hereford, J. Plescia, and M. Ort (2006), Multiple constraints on the age of a Pleistocene lava dam across the little Colorado River at Grand Falls, Arizona, *Geol. Soc. Am. Bull.*, *118*(3–4), 421–429, doi:10.1130/B25814.1.
- Dupré, B., C. Dessert, P. Oliva, Y. Godderis, J. Viers, L. Francois, R. Millot, and J. Gaillardet (2003), Rivers, chemical weathering and earth's climate, *C. R. Geosci.*, *335*(16), 1141–1160, doi:10.1016/j.crte.2003.09.015.
- Gaillardet, J., B. Dupre, P. Louvat, and C. J. Allegre (1999), Global silicate weathering and CO₂ consumption rates deduced from the chemistry of large rivers, *Chem. Geol.*, *159*(1–4), 3–30, doi:10.1016/S0009-2541(99)00031-5.
- Gevaert, A. I., et al. (2014), Hillslope-scale experiment demonstrates the role of convergence during two-step saturation, *Hydrol. Earth Syst. Sci.*, *18*(9), 3681–3692, doi:10.5194/hess-18-3681-2014.
- Gislason, S. R., and S. Arnorsson (1993), Dissolution of primary basaltic minerals in natural-waters—Saturation state and kinetics, *Chem. Geol.*, *105*(1–3), 117–135, doi:10.1016/0009-2541(93)90122-Y.
- Gislason, S. R. and E. H. Oelkers (2003), Mechanism, Rates, and consequences of basaltic glass dissolution: II. An experimental study of the dissolution rates of basaltic glass as a function of pH and temperature, *Geochim. Cosmochim. Acta*, *67*(20), 3817–3832, doi:10.1016/S0016-7037(00)00176-5.
- Gislason, S. R., S. Arnorsson, and H. Armannsson (1996), Chemical weathering of basalt in Southwest Iceland: Effects of runoff, age of rocks and vegetative/glacial cover, *Am. J. Sci.*, *296*(8), 837–907.
- Gislason, S. R., et al. (2009), Direct evidence of the feedback between climate and weathering, *Earth Planet. Sci. Lett.*, *277*(1–2), 213–222, doi:10.1016/j.epsl.2008.10.018.
- Goldberg, S., and G. Sposito (1984), A Chemical-Model of Phosphate Adsorption by Soils. 1. Reference oxide minerals, *Soil Sci. Soc. Am. J.*, *48*(4), 772–778.
- Gurumurthy, G. P., K. Balakrishna, J. Riotte, J.-J. Braun, S. Audry, H. N. Udaya Shankar, and B. R. Manjunatha (2012), Controls on intense silicate weathering in a tropical river, Southwestern India, *Chem. Geol.*, *300*, 61–69, doi:10.1016/j.chemgeo.2012.01.016.

- Hopp, L., C. Harman, S. L. E. Desilets, C. B. Graham, J. J. McDonnell, and P. A. Troch (2009), hillslope hydrology under glass: Confronting fundamental questions of soil-water-biota co-evolution at Biosphere 2, *Hydrol. Earth Syst. Sci.*, *13*(11), 2105–2118, doi:10.5194/hess-13-2105-2009.
- Louvat, P., and C. J. Allègre (1997), Present denudation rates on the island of reunion determined by river geochemistry: Basalt weathering and mass budget between chemical and mechanical erosions, *Geochim. Cosmochim. Acta*, *61*(17), 3645–3669, doi:10.1016/S0016-7037(97)00180-4.
- Lumsdon, D. G. and V. C. Farmer (1995), Solubility characteristics of proto-imogolite sols: How silicic acid can de-toxify aluminium solutions, *Eur. J. Soil Sci.*, *46*(2), 179–186, doi:10.1111/j.1365-2389.1995.tb01825.x.
- Navarre-Sitchler, A., and S. Brantley (2007), Basalt weathering across scales, *Earth Planet. Sci. Lett.*, *261*(1–2), 321–334, doi:10.1016/j.epsl.2007.07.010.
- Nesbitt, H. W., and R. E. Wilson (1992), Recent chemical-weathering of basalts, *Am. J. Sci.*, *292*(10), 740–777.
- Niu, G.-Y., et al. (2014), Incipient subsurface heterogeneity and its effect on overland flow generation—Insight from a modeling study of the first experiment at the Biosphere 2 landscape evolution observatory, *Hydrol. Earth Syst. Sci.*, *18*(5), 1873–1883, doi:10.5194/hess-18-1873-2014.
- Oelkers, E. H. (2001), General kinetic description of multioxide silicate mineral and glass dissolution, *Geochim. Cosmochim. Acta*, *65*(21), 3703–3719, doi:10.1016/S0016-7037(01)00710-4.
- Oelkers, E. H., and S. R. Gislason (2001), The mechanism, rates and consequences of basaltic glass dissolution: I. An experimental study of the dissolution rates of basaltic glass as a function of aqueous Al, Si and oxalic acid concentration at 25° C and pH = 3 and 11, *Geochim. Cosmochim. Acta*, *65*(21), 3671–3681, doi:10.1016/S0016-7037(01)00664-0.
- Pangle, L. A., et al. (2015), The Landscape Evolution Observatory: A Large-Scale Controllable Infrastructure to Study Coupled Earth-Surface Processes, *Geomorphology*, *244*, 190–203.
- Parfitt, R. L. (1989), Phosphate reactions with natural allophane, ferrihydrite and goethite, *J. Soil Sci.*, *40*(2), 359–369.
- Steele, C. L., and P. van Cappellen (1990), A new kinetic approach to modeling water-rock interaction—The role of nucleation, precursors, and ostwald ripening, *Geochim. Cosmochim. Acta*, *54*(10), 2657–2677, doi:10.1016/0016-7037(90)90003-4.
- Stefansson, A. and S. R. Gislason (2001), Chemical weathering of basalts, Southwest Iceland: Effect of rock crystallinity and secondary minerals on chemical fluxes to the ocean, *Am. J. Sci.*, *301*(6), 513–556, doi:10.2475/ajs.301.6.513.
- Stumm, W. (1997), Reactivity at the mineral-water interface: Dissolution and inhibition, *Colloids Surf. A*, *120*(1–3), 143–166, doi:10.1016/S0927-7757(96)03866-6.
- Stumm, W., and J. J. Morgan (1996), *Aquatic Chemistry: Chemical Equilibria and Rates in Natural Waters*, Environmental Science and Technology, 3rd ed., John Wiley, N. Y.
- Suchet, P. A., J. L. Probst, and W. Ludwig (2003), Worldwide distribution of continental rock lithology: Implications for the atmospheric/soil CO₂ uptake by continental weathering and alkalinity river transport to the oceans, *Global Biogeochem. Cycles*, *17*(2), 1038, doi:10.1029/2002GB001891.
- Swoboda-Colberg, N. G., and J. I. Drever (1993), Mineral dissolution rates in plot-scale field and laboratory experiments, *Chem. Geol.*, *105*(1–3), 51–69.
- Tebo, B. M., J. R. Bargar, B. G. Clement, G. J. Dick, K. J. Murray, D. Parker, R. Verity, and S. M. Webb (2004), Biogenic manganese oxides: Properties and mechanisms of formation, *Annu. Rev. Earth Planet. Sci.*, *32*, 287–328.
- Tetzlaff, D., J. Seibert, K. J. McGuire, H. Laudon, D. A. Burn, S. M. Dunn, and C. Soulsby (2009), How does landscape structure influence catchment transit time across different geomorphic provinces?, *Hydrol. Processes*, *23*(6), 945–953, doi:10.1002/hyp.7240.
- Torn, M. S., S. E. Trumbore, O. A. Chadwick, P. M. Vitousek, and D. M. Hendricks (1997), Mineral control of soil organic carbon storage and turnover, *Nature*, *389*(6647), 170–173, doi:10.1038/38260.
- van Emmerik, Tristan J., D. E. Sandstrom, O. N. Antzutkin, M. J. Angove, and B. B. Johnson (2007), P-31 solid-state nuclear magnetic resonance study of the sorption of phosphate onto gibbsite and kaolinite, *Langmuir*, *23*(6), 3205–3213, doi:10.1021/la062765b.
- White, A. F., and M. L. Peterson (1990), Role of reactive-surface-area characterization in geochemical kinetic-models, *ACS Symp. Ser.*, *416*, 461–475.
- Whittig, L. D., W. R. Allardice, and A. Klute (1986), *Methods of Soil Analysis: Part 1—Physical and Mineralogical Methods, X-Ray Diffraction Techniques*, SSSA Book Ser., *5.1*, 331–362, doi:10.2136/sssabookser5.1.2ed.c12.
- Wolff-Boenisch, D., S. R. Gislason, E. H. Oelkers, and C. V. Putnis (2004), The dissolution rates of natural glasses as a function of their composition at pH 4 and 10.6 and temperatures from 25 to 74 degrees C, *Geochim. Cosmochim. Acta*, *68*(23), 4843–4858, doi:10.1016/j.gca.2004.05.027.
- Zhang, H. L., P. R. Bloom, and E. A. Nater (1993), Change in surface-area and dissolution rates during hornblende dissolution at pH 4.0, *Geochim. Cosmochim. Acta*, *57*(8), 1681–1689.

Erratum

In the originally published version of this article, there was an error in the dissolution reactions written for the first two chemical reactions in Table 3. The table has since been corrected and this version may be considered the authoritative version of record.